

JGR Space Physics

RESEARCH ARTICLE

10.1029/2019JA027326

Key Points:

- Instability growth differs between 2-D and 3-D simulations
- Saturated density in 3-D spectra are flat above peak wavelength and fall off sharoly below
- The variation of relative plasma drift with altitude largely controls the variation in flow angle

Supporting Information:

- · Supporting Information \$1
- Movie S1
- Movie S2
- Movie S3
- Movie \$4
- Movie S5
 Movie S6

Correspondence to:

M. A. Young, myoung.space.science@gmail.com

Citation:

Young, M. A., Oppenheim, M. M., & Dimant, Y. S. (2020). The farley-buneman spectrum in 2-D and 3-D PIC simulations. Journal of Geophysical Research: Space Physics, 125, e2019JA027326. https://doi.org/ 10.1029/2019JA027326

Received 20 AUG 2019 Accepted 8 DEC 2019 Accepted article online 3 JAN 2020

The Farley-Buneman Spectrum in 2-D and 3-D Particle-in-Cell Simulations

Matthew A. Young^{1,2}, Meers M. Oppenheim¹, and Yakov S. Dimant¹

¹Center for Space Physics, Boston University, Boston, MA, USA, ²Space Science Center, University of New Hampshire, Durham, NH, USA

Abstract Since the 1960s, the Farley-Buneman instability has played an important role in probing the E-region ionosphere. The intervening years have seen significant progress in the linear theory of this instability, its relation to other instabilities, and some of its observational signatures. However, the saturation mechanism and nonlinear behavior remain open topics because of their role in controlling energy flow in the E-region plasma. This paper explores the saturated state of the Farley-Buneman instability in 2-D and 3-D kinetic simulations of the high-latitude ionosphere, at three different simulated altitudes: 107, 110, and 113 km. These simulations show irregularity amplitude growth and saturation in all runs, but irregularity growth takes much longer in 2-D than in 3-D. Once the simulations reach saturation, wave power in the meter-scale regime falls off as a power law below the wavelength of peak growth, but the power law index is larger in 3-D than in 2-D. At longer wavelengths, the 3-D spectrum is much flatter than the 2-D spectrum. This implies that purely 2-D simulations of the Farley-Buneman instability may overestimate irregularity amplitudes at decameter scales and may also underestimate the efficiency of ion Landau damping at the ion mean-free-path scale. From a physical perspective, the relatively flat spectra above the wavelength of peak growth in 3-D simulations imply a wavelength-independent saturation mechanism across a range of altitudes. Finally, both 2-D and 3-D simulations demonstrate the importance of accounting for zeroth-order ion drift when estimating the flow angle of density irregularities.

Plain Language Summary At approximately 90–120 km in altitude, the Earth's atmosphere comprises a gas containing mostly neutral molecules, and a small number of positively charged ions and electrons. This sort of gas is called a weakly ionized plasma. Aeronomy researchers have known for decades that the weakly ionized plasma around 90–120 km in Earth's atmosphere can grow unstable and reflect radio waves, and they have used radio-wave reflection as one technique to probe this region of geospace. However, the aeronomy community still does not understand the nature of the fully developed plasma instabilities in this region. This work addresses that problem with computer simulations. It finds that 2-D simulations do not capture all the characteristics of 3-D simulations, which should mimic reality more closely. It also finds that whatever mechanism creates the fully developed 3-D instability should apply to wavelengths from a few meters to tens of meters. Finally, this work suggests that the direction along which the unstable waves travel should change in a predictable way as altitude increases. These conclusions will help future researchers estimate atmospheric parameters based on radar and rocket measurements.

1. Introduction

During periods of elevated geomagnetic activity, strong field-aligned currents close through the E-region, where they drive comparably strong Hall currents. Electrons in these Hall currents stream through the less-mobile ions at speeds larger than the plasma acoustic speed, setting up the conditions for the Farley-Buneman instability (FBI) (Buneman, 1963; Farley, 1963b, 1963a). The FBI is responsible for anomalous transport across the magnetic field, elevated electron temperatures, and increased conductivity.

The FBI requires an electron-ion relative drift speed above a certain threshold (cf. Dimant & Oppenheim, 2011b; Makarevich, 2016b). Electrons are magnetized above roughly 80 km, so their drift velocity is effectively $E_0 \times B_0/B_0^2$ throughout the E-region. Ions are strongly demagnetized via collisions in the lower to middle E-region and drift very slowly in the direction of E_0 , causing the relative drift velocity to be very nearly equal to the electron drift velocity at those altitudes. However, ion collision frequencies decrease with

©2020. American Geophysical Union. All Rights Reserved.

YOUNG ET AL. 1 of 15



altitude, causing their drifts to become appreciable and thereby causing the magnitude and direction of the electron-ion relative drift to deviate significantly from $E_0 \times B_0/B_0^2$.

The present work demonstrates the evolution of FBI irregularities in 2-D and 3-D simulations of the auroral E-region ionosphere during a period of moderately strong electric field, at altitudes where the ion drift is not negligible. Knowledge of the growth and saturation of the FBI during periods of increased auroral activity can provide information about the ionosphere's role in mediating magnetosphere-ionosphere coupling during increased geomagnetic activity. The results of these simulations should help observers estimate large-scale parameters (e.g., the background electric field) from small-scale measurements.

Interest in the radar aurora dates back to 1937, when Eckersley (1937) showed that a sufficiently strong HF radio apparatus could observe radar echoes associated with the visible aurora. Since then, the aeronomy community has produced a substantial amount of observational and theoretical work on the subject of E-region coherent echoes. See the excellent reviews of the radar aurora by Makarevich (2009) and Hysell (2015) and of E-region instabilities in general by Fejer and Kelley (1980), Sahr and Fejer (1996), and Farley (2009) for more information.

Bowles (1954) used a 25.4 MHz radar to study auroral echoes and determine that the radar aurora is highly aligned with the background magnetic field. Booker (1956) established that auroral radar echoes come from field-aligned irregularities (FAI) in the electron density, with scale sizes on the order of a meter perpendicular to \mathbf{B}_0 and 5 to 10 m parallel to \mathbf{B}_0 .

Much of the initial work in characterizing E-region density irregularities began at the geomagnetic equator (Bowles et al., 1960, 1963; Cohen & Bowles, 1963), but Haldoupis (1989) acknowledged that most of the outstanding questions posed by auroral observations seemed to have no equatorial counterpart. In particular, he called out the importance of altitude in instability generation and saturation mechanisms.

Numerous rocket missions have provided in situ measurements of the auroral plasma environment. Måseide et al. (1973) observed electric field fluctuations that increased in the presence of enhanced auroral emission. Kelley and Mozer (1973) observed dispersionless electrostatic waves during a strong substorm whereas Iranpour et al. (1997) observed dispersive waves in which longer wavelengths had lower speed but which propagated with the Hall current regardless of wavelength.

Pfaff et al. (1984) reported simultaneous in situ electric field and density measurements in the presence of a 54 mV/m background electric field. Those measurements showed signatures of both meter-scale FBI and longer-wavelength gradient drift instability (GDI) effects, evidenced by a broad spectrum and a reduction in long-wavelength power as conditions became unfavorable to the GDI. The authors reported a wave power spectrum that was a strong function of wave number and the presence of secondary waves propagating perpendicular to the direction of primary irregularities.

The Scandinavian Twin Aurora Radar Experiment (STARE) and the Sweden And Britain Radar Experiment (SABRE) provided a large body of observations of coherent echoes from the auroral E-region. In their review of the combined STARE/SABRE campaigns, Nielsen and Schmidt (2014) noted that studying the radar aurora gained popularity when researchers discovered that the back-scattered signal contained information about the background electric field.

The E-region Rocket/Radar Instability Study (ERRRIS) campaign (Pfaff et al., 1992; Sahr et al., 1992) comprised three rocket flights with ground-based support from STARE, the European Incoherent Scatter (EISCAT) radar, and the Cornell University Portable Radar Interferometer (CUPRI). Rocket-based measurements of electric field and density fluctuations suggested that the background electric field controls the amplitude of FBI irregularities, the shortest wavelength to which their spectrum extends, and the altitude range over which they are present.

Common volume measurements by STARE and EISCAT showed that estimates of electron drift from STARE observations of coherent echoes are reasonably good as long as the electron drift is not too large (Nielsen & Schlegel, 1983). Similar measurements also showed that the phase speed as a function of electron drift speed follows the ion acoustic speed (Nielsen & Schlegel, 1985), which has been a consistent result of both auroral and equatorial FBI observations. In both studies, the dual-beam STARE system allowed researchers to measure the irregularity phase velocity in two directions and to infer the echoing altitude, while EISCAT provided estimates of the electron drift velocity by measuring F-region plasma drifts. The angle between

YOUNG ET AL. 2 of 15



these two drifts is the flow angle. Knowing how the flow angle changes with altitude can help observers to estimate the electric field in the E-region through coherent backscatter alone.

Haldoupis et al. (1984) also used STARE to make observations of a common volume in the high-latitude E-region. Those authors observed narrow and broad Doppler spectra in the same volume, with narrow spectra coming from flow angles within -60° to 0° and broad spectra coming from flow angles within -90° to -65° . They attributed the simultaneous narrow and broad spectra to collocated primary and secondary irregularities driven by the FBI and the related GDI. Dimant and Oppenheim (2011a) demonstrated how these secondary irregularities constitute a nonlinear current that has significant implications for E-region conductivities during periods of intense geomagnetic activity.

Hysell et al. (2012) reported results from VHF coherent-scatter radar observations during a geomagnetic substorm over Alaska, with an emphasis on aspects of the radar aurora revealed through VHF radar imaging. One goal of that work was to establish a relationship between coherent backscatter from FAI and F-region $E_0 \times B_0$ drifts, so that future research could use the former to predict the latter. In order to compare E-region coherent-scatter measurements to F-region incoherent-scatter measurements, they first assumed that the F-region electric field maps perfectly down magnetic field lines into the E-region. They also assumed that the coherent-scatter Doppler velocity and spectral width followed empirical formulas involving the electron drift speed, the ion acoustic speed, the LOS E-region ion drift speed, the flow angle, and an angular correction for wave turning. They set the latter parameter to 10° and assumed that the observed echoes came from 110 km.

The angular correction for wave turning in Hysell et al. (2012) reflects a phenomenon central to the present paper. A joint STARE/EISCAT study by Uspensky et al. (2003) emphasized the importance of accounting for non-negligible ion drifts and reported a resultant deflection of the phase velocity from $E_0 \times B_0$ by 5° to 15°. A theoretical paper by St.-Maurice and Hamza (2001) proposed a nonlinear fluid theory of E-region irregularities which did not resort to the usual assumption of superimposed plane waves and explained wave turning as a natural consequence of a rotating electric field in plasma holes and blobs. Janhunen (1994a, 1994b) concluded that the flow angle offset from $E_0 \times B_0$ was responsible for instability saturation in his particle-in-cell (PIC) simulations. Oppenheim and Dimant (2004), Oppenheim et al. (2008), and Oppenheim and Dimant (2013) attributed wave turning in their PIC simulations to thermal effects described by Dimant and Oppenheim (2004).

The work by Haldoupis et al. (1984) and Hysell et al. (2012) illustrates the value of knowing, or at least accurately estimating, the flow angle of density irregularities. Wave turning in simulations demonstrates the tenuousness of assuming that E-region density irregularities propagate in the direction of electron drift, and the work by Uspensky et al. (2003) further emphasizes the role of ion drifts. Rocket-borne measurements of density and electric field corroborate the ground-based observations of FBI-driven irregularities in the presence of strong auroral electric fields and demonstrate that "the unstable auroral E-region is far from being a layer of homogeneous turbulence" (Pfaff et al., 1984).

This paper proceeds as follows: Section 2 describes the relevant instability theory. Section 3 describes the simulation method. It also explains relevant physical parameters while acknowledging drawbacks and assumptions. Section 4 presents the simulation results in terms of RMS density perturbations (section 4.1) and irregularity flow angle (section 4.2). Section 5 discusses the results with respect to previously published theory and observation. Section 6 summarizes the paper.

2. Theory

The FBI occurs in a warm plasma with magnetized electrons and collisionally demagnetized ions. Formally, that means the magnitude of the electron cyclotron frequency, Ω_e , is greater than the electron collision frequency, v_e , whereas $\Omega_I < v_I$ for ions. This work uses the magnetization parameter for species s: $\kappa_s \equiv \Omega_s/v_s$. The presence of an electric field, typically due to winds (at equatorial latitudes), field-aligned currents (at high latitudes), or plasma gradients, causes electrons to stream through ions. The electrostatic force between electrons and ions imparts momentum to the ions that competes with thermal pressure when random density perturbations arise. When the total electric field exceeds a threshold value, the kinetic pressure due to ion inertia overcomes thermal pressure and perturbations grow (Dimant & Sudan, 1995). The linear fluid theory of the FBI is well established in the literature (Fejer & Kelley, 1980), and recent work has advanced

YOUNG ET AL. 3 of 15

Table 1 Simulation Parameters								
Symbol	Value	Unit	Name					
m_l	5.0×10^{-26}	kg	Ion mass					
m_i/m_e	1250		Mass ratio					
m_n	4.6×10^{-26}	kg	Neutral mass					
T_n	300	K	Neutral temperature					
n_0	2×10^{8}	m^{-3}	Plasma density					
$v_{l:sim}$	1022, 611, 369	s^{-1}	Ion-neutral coll. freq.					
v _{e:sim}	965, 671, 491	s^{-1}	Elecneutral coll. freq.					
$\psi_{\perp:stm}$	0.030 , 0.013 , 5.6×10^{-3}		Anisotropy factor					
h	107, 110, 113	km	Effective altitude					
B_{20}	5.0×10^{-5}	T	Magnetic field					
E_{y0}	50.0	mV/m	Electric field					
L_{χ}	40.96	m	Box length in X direction					
dx	0.04, 0.08	m	2-D, 3-D cell size in X direction					
L_y	40.96	m	Box length in Y direction					
dy	0.04, 0.08	m	2-D, 3-D cell size in Y direction					
L_{z}	163.84	m	Box length in Z direction					
dz	0.08	m	3-D cell size in Z direction					
L_t	≈ 460, ≈ 115	ms	2-D, 3-D time span					
dt	1.75×10^{-6} , 3.0×10^{-6}	S	2-D, 3-D time step					

the community's understanding of its connection to the linear fluid theory of other ionospheric instabilities (Dimant & Oppenheim, 2011b; Makarevich, 2016a, 2016b, 2019). In the absence of a background density gradient, the real frequency and growth rate are

$$\omega_r = \frac{\mathbf{k} \cdot \mathbf{u}_d}{1 + w} + \mathbf{k} \cdot \mathbf{u}_{i0}, \qquad (1)$$

$$\omega_{l} = \frac{\psi}{1 + \psi} \left(\frac{\omega_{r}^{2} - k^{2}C_{s}^{2}}{\nu_{i}} \right), \tag{2}$$

where **k** is the wave vector with wave number $k=2\pi/\lambda$, $\mathbf{u}_d\equiv\mathbf{u}_{e0}-\mathbf{u}_{i0}$ is the zeroth-order electron-ion relative drift velocity, \mathbf{u}_{e0} and \mathbf{u}_{i0} are the zeroth-order drift velocities of electrons and ions, $C_s\equiv\sqrt{(T_i+T_e)/m_i}$ is the sound speed with temperature in energy units, and

$$\psi \equiv \psi_{\perp} \left[\left(\frac{k_{\perp}}{k} \right)^2 + \left(\frac{\kappa_e k_{\parallel}}{k} \right)^2 \right], \qquad \psi_{\perp} \equiv \frac{1}{\kappa_e \kappa_l}.$$

The ψ parameter is essentially a measure of the anisotropy in electron and ion mobilities.

Isothermal linear theory predicts a threshold value of $E_{th} = B_0 C_s (1 + \psi)$, where B_0 is the background magnetic field. At E-region altitudes, the dominant neutral species is N_2 and the dominant ion is NO⁺. Collisions of NO⁺ with N_2 are effectively nonresonant Maxwell molecule interactions (i.e., elastic collisions for which v_t is independent of velocity), so their collision frequency depends only on neutral density. Collisions of e⁻ with N_2 are inelastic. They depend on neutral density and electron temperature, since an increase in thermal energy will disproportionately increase the velocity of the less massive electrons relative to the neutrals (Schunk & Nagy, 2004).

3. Simulation Methods and Limitations

The simulations presented herein employed the full particle-in-cell (PIC) version of the electrostatic parallel particle-in-cell (EPPIC) numerical code. See Oppenheim and Dimant (2004) for a description of the advantages and disadvantages of the full PIC version of the code, see Oppenheim et al. (2008) for a description of

YOUNG ET AL. 4 of 15

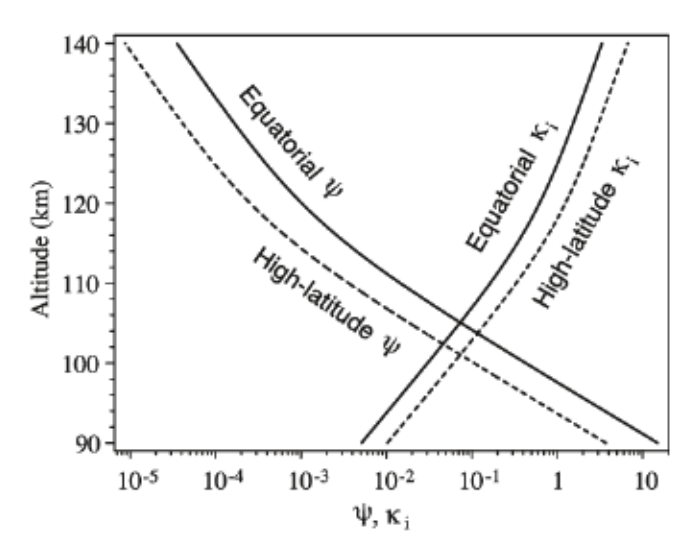


Figure 1. Figure 2 from Dimant and Oppenheim (2004), showing theoretical altitudinal profiles of ψ_{\perp} and κ_{I} at equatorial and high magnetic latitudes.

an improvement in parallelizing the 2-D version, and see Oppenheim and Dimant (2013) for a description of the 3-D version. Table 1 lists the simulation parameters used in the present work.

The ratio of ion mass to electron mass was artificially small for these simulation runs—a common practice in PIC simulations. Oppenheim and Dimant (2004) noted that the simulation can use an artificially inflated electron mass as long as it maintains the electron and ion Hall and Pedersen drift rates, and the collision and thermalization rates. It must also keep the electron collision frequency large compared to the ion collision frequency, so that electron Landau damping does not become important.

The simulation used a plasma density, n_0 , appropriate to the night time E-region. This not only mimics auroral conditions; it also reduces the electron plasma frequency, $\omega_{pe} \sim \sqrt{n_0}$, which allows the simulation to take larger time steps. The FBI growth rate does not depend on the total density, provided the density satisfies the condition $\omega_{pi}/v_l > 1$ (Rosenberg & Chow, 1998).

In this work, $m_{e:sim}$ represents the simulated electron mass. Various quantities, described below, must be adjusted self-consistently in order to compensate for the artificially inflated electron mass. In each case, the subscript sim will denote a simulated quantity which differs in general from the physical value.

A major focus of this work is the change in instability behavior with altitude. Neutral density is a good proxy for altitude in the atmosphere, but EPPIC does not use neutral density as a simulation parameter, so the simulated ion and electron collision frequencies, $v_{t:stm}$ and $v_{e:stm}$, specify the equivalent altitude. As Oppenheim and Dimant (2013) explain, the effective collision frequency during a simulation run typically differs from the input value. Selecting an input value that will produce an appropriate simulated value requires some care.

Figure 2 in Dimant and Oppenheim (2004), reproduced here in Figure 1, provides a way to select collision frequencies corresponding to a desired altitude. The first step is to identify an appropriate value of $\psi_{\perp:sim}$ for the desired altitude. Next, the user identifies the corresponding value of $\kappa_{1:sim} = \Omega_t/\nu_{t:sim}$ from which they calculate $\nu_{t:sim}$. The user then calculates $\nu_{e:sim}$ from the definition $\psi_{\perp} \equiv \nu_e \nu_i/\Omega_e \Omega_i$:

$$v_{e:sim} = \psi_{\perp:sim} \left(\frac{\Omega_i \Omega_{e:sim}}{v_{i:sim}} \right), \tag{3}$$

$$= \psi_{\perp:sim} \left(\frac{q_1 q_e B_0^2}{m_l m_{e:sim} v_{l:sim}} \right). \tag{4}$$

As described above, a sim subscript denotes a simulated value. These values differ in general from physical values in order to compensate for the artificially inflated electron mass.

With these candidate values for $v_{i:sim}$ and $v_{e:sim}$ in hand, the user typically runs two types of simulations with subthreshold electric fields to validate their values. The process for validating $v_{i:sim}$ consists of running the simulator with a subthreshold driving electric field, $E_{y0} \approx 10$ mV/m, and calculating the effective ion collision frequency from the ion Pedersen drift, u_{iP} , via the zeroth-order drift relation $v_{i:sim} = q_i E_{y0}/m_i u_{iP}$. The process for validating $v_{e:sim}$ consists of running the simulator with a small parallel electric field, $E_{\parallel 0} \approx 0.1$ mV/m and calculating the effective electron collision frequency from the electron parallel drift, $u_{e\parallel}$: $v_{e:sim} = |q_e|E_{\parallel 0}/m_e u_{e\parallel}$.

Many observations of FBI associated with the aurora assume that the echoes originate in a volume centered on 110 km. The effectively altitudes of the simulations presented here encompass that altitude to facilitate comparison to observations. The present simulations used three pairs of effective collision frequencies: $v_{i:sim} = 1,022 \text{ s}^{-1}$ and $v_{e:sim} = 965 \text{ s}^{-1}$, corresponding to 107 km; $v_{i:sim} = 610 \text{ s}^{-1}$ and $v_{e:sim} = 671 \text{ s}^{-1}$, corresponding to 110 km; and $v_{i:sim} = 369 \text{ s}^{-1}$ and $v_{e:sim} = 491 \text{ s}^{-1}$, corresponding to 113 km. Note that $v_{e:sim} \approx v_{i:sim}$ here, whereas $v_e \approx 10v_t$ in the real E-region.

YOUNG ET AL. 5 of 15

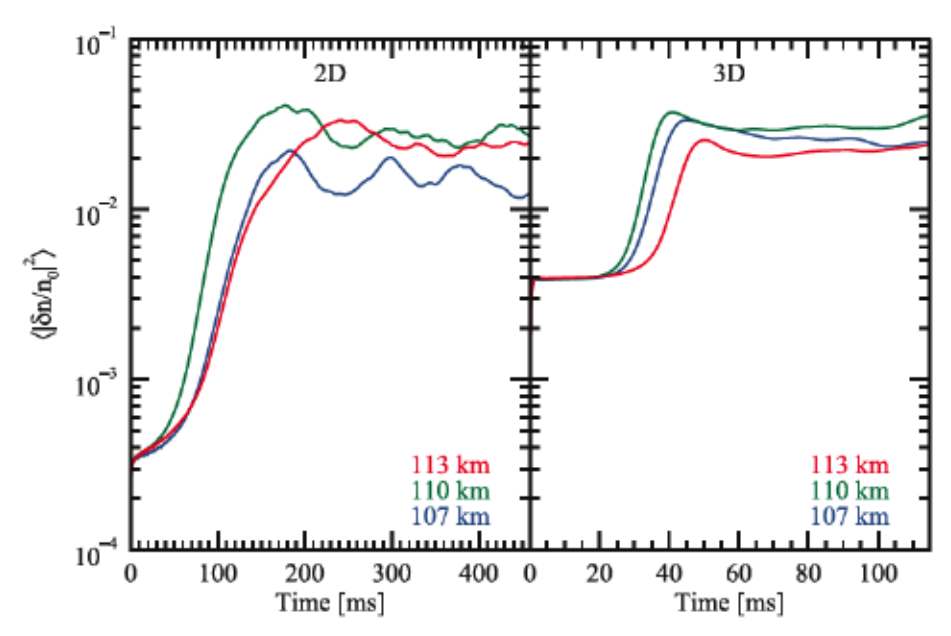


Figure 2. Mean squared amplitude of density perturbations at all wavelengths. The left panel shows 2-D runs and the right panel shows 3-D runs. The blue traces correspond to 107 km, the green traces correspond to 110 km, and the red traces correspond to 113 km.

The EPPIC collision routines calculate the ratio of the particle velocity to a reference velocity and then check that ratio against a normalized random number to calculate the probability of collision. The reference velocity depends on the species' initial thermal velocity. The FBI dramatically heats the local plasma (Oppenheim & Dimant, 2013), so the simulation runs presented here seeded both species' populations with high temperatures to ensure that the collision model would behave accurately as the plasma heats up. In 2-D and 3-D runs, both species cooled rapidly, then heated, and finally leveled off at elevated temperatures. Electron temperatures at the end of 3-D runs were in the range 500–800 K, which represents modest heating compared to the temperatures observed, for example, by St.-Maurice et al. (1981) and Foster and Erickson (2000).

The dimensionless parameter $\Theta_0 \equiv \sqrt{m_e v_e/m_i v_i}$ controls the aspect angle of peak growth in 3-D (Oppenheim & Dimant, 2004). In nature, its value is approximately 1.4×10^{-2} radians, or 0.8° . The method described above for selecting collision attempts to keep $m_{e:sim}v_{e:sim} \approx m_e v_e$ in order to maintain realistic electron mobilities despite the artificially high electron mass. Thus, these simulations should produce physically reasonable growth-stage aspect angles. However, the discretization of these simulations does not resolve parallel modes well, so conclusions about irregularity aspect angles are approximate at best.

This work follows radar convention by defining flow angle as the angle between zeroth-order electron drift and LOS. Since electrons drift predominantly in the $\mathbf{E}_0 \times \mathbf{B}_0$ direction and radars can only observe Doppler shift from echoes propagating parallel or antiparallel to their LOS, the flow angle is equivalently the angle between $\mathbf{E}_0 \times \mathbf{B}_0$ and the direction of wave propagation. Where the sign of flow angle is unspecified, the reader may assume that it is negative in a counter-clockwise sense. In terms of physical quantities, it points in a direction between $\mathbf{E}_0 \times \mathbf{B}_0$ and $-\mathbf{E}_0$.

4. Results

This section presents the main results from 2-D and 3-D simulations. Section 4.1, presents two views of spectral data averaged around all angles in the perpendicular plane, to illustrate the stages of instability development. This analysis uses a coordinate system with k_{\parallel} parallel to \mathbf{B}_0 (the parallel direction), k_{Pod} parallel to \mathbf{E}_0 (the Pedersen direction), and k_{Hall} parallel to $\mathbf{E}_0 \times \mathbf{B}_0$ (the Hall direction). Section 4.2 presents images of spectral amplitude in the perpendicular plane to illustrate the dependence of flow angle on altitude.

4.1. RMS Density Perturbations

Figure 2 shows $\langle |\delta n/n_0|^2 \rangle$ for all perturbations throughout both the 2-D and 3-D simulations. Here, $\langle |\delta n/n_0|^2 \rangle$ is the squared RMS perturbed density as a function of time. The final values correspond to

YOUNG ET AL. 6 of 15

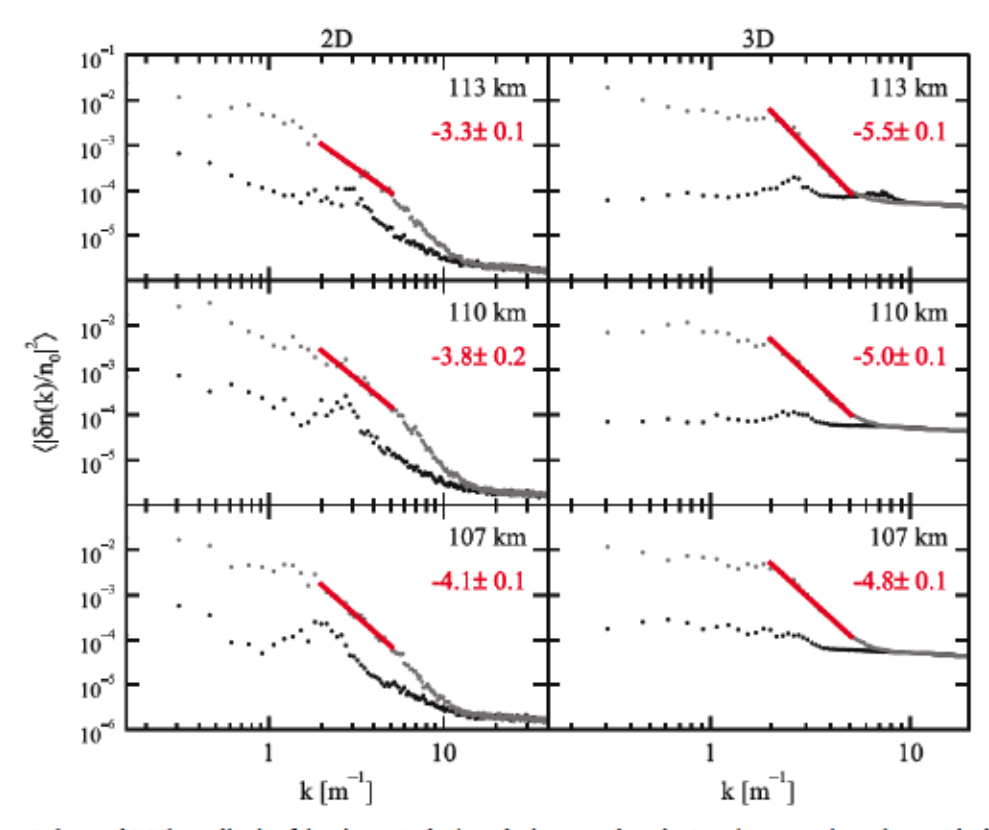


Figure 3. Squared RMS amplitude of density perturbations during growth and saturation stages in each run. The left panels correspond to 2-D runs and the right panels to 3-D runs. Gray traces show the growth-stage spectrum, and black stages show the saturated spectrum. Red lines show a power law fit to the meter-scale range of the saturated spectrum, and the printed number gives the slope.

perturbation amplitudes of approximately 11% and 15%, which is typical for the moderately to strongly driven FBI.

All runs exhibit a growth stage followed by a saturation stage. The run at 110 km grows most quickly in both 2-D and 3-D, though the discrepancy is greater in 2-D. The 2-D run at 107 km saturates at a lower amplitude than the other two. Despite the slower growth at 113 km than at 110 km, both runs saturate at roughly the same amplitude. Growth in the 3-D run at 113 km starts about 10 ms later than in the other two runs and reaches a slightly lower initial saturation amplitude. While the 3-D run at 107 km largely mimics the run at 110 km during growth and initial saturation stages, its amplitude drops to the level of the run at 113 km by the end. However, the difference is less than a factor of two. For the most part, all runs, especially those in 3-D, saturate at approximately the same amplitude.

It is interesting that the saturated amplitude is nearly independent of altitude, especially in 3-D. This implies that the mechanism which saturates linear growth is nearly independent of ion mean free path, since that parameter sets the effective altitude in these simulations. However, there are small difference between saturation amplitudes, which may result from different heating rates at all three altitudes. The saturation amplitude in all 2-D runs actually oscillates about a mean value, whereas it oscillates very weakly, if at all, in 3-D runs. Plots of temperature (not shown) show very similar oscillations, or lack thereof, in 2-D and 3-D runs.

Figure 3 presents a view of $\langle |\delta n(k)/n_0|^2 \rangle$ versus wave number during irregularity growth and after instability saturation in each run. Table 2 lists the times (in milliseconds) corresponding to growth-stage and saturated-stage traces. The supporting information accompanying this paper includes movies of all six spectra as a function of time.

During the linear growth stage, 3-D simulations show growth predominantly at a small range of wavelengths whereas 2-D simulations show a more complex pattern of growth over a broader range of wavelengths.

YOUNG ET AL. 7 of 15

Table 2 Spectral Snapshot Times (ms)									
	2-D			3-D					
	107 km	110 km	113 km	107 km	110 km	113 km			
Growth	78.85	78.85	111.10	30.46	25.09	30.46			
Saturated	458.75	458.75	458.75	114.69	114.69	114.69			

All runs exhibit initial growth at a wavelength of a few meters, but the peak is broader and higher in 2-D than in 3-D. In 2-D runs, $\langle |\delta n(k)/n_0|^2 \rangle$ falls off on both sides of the peak but increases again toward longer wavelengths. In 3-D runs, $\langle |\delta n(k)/n_0|^2 \rangle$ falls off toward wavelengths shorter than the peak at all altitudes and falls off toward longer wavelengths at 110 and 113 km. Despite the relative increase at longer wavelengths at 107 km, $\langle |\delta n(k)/n_0|^2 \rangle$ is still lower than in 2-D runs. The run at 113 km also has a secondary peak at a wavelength less than a meter.

Following the linear growth stage, all runs transition to a saturated state characterized by increased long-wavelength growth. The 2-D saturated spectra show a power law dependence on k with slopes from -3.3 to -4.1 in the meter-scale range and a smooth transition to a shallower slope with decreasing k. Mean squared amplitude is at least an order of magnitude larger at the longest wavelengths, compared to the wavelength of peak initial growth. The 3-D saturated spectra show an even more distinct power law, with a knee near k=2 m⁻¹. The 3-D power law slopes in the meter-scale regime are steeper in 3-D than in 2-D, ranging from -4.8 to -5.5, and the long-wavelength spectra are flatter than in 2-D.

4.2. Flow Angle

Quantifying the flow angle of density perturbations in the E-region ionosphere is crucial to using their drift speed to estimate the driving electric field. The following analysis presents 2-D images of density perturbation spectra in the plane perpendicular to ${\bf B}_0$. Images from 3-D runs include the same 4-point k_{\parallel} average described in 4.1 and are therefore quasi-perpendicular spectra.

In an isothermal plasma, the linear fluid theory of the FBI predicts that density irregularities will propagate parallel to the electron-ion relative drift. However, the plasma is decidedly *not* isothermal during geomagnetically disturbed conditions. In addition to extreme electron heating (cf. Foster & Erickson, 2000; Oppenheim & Dimant, 2013; Schlegel & St.-Maurice, 1981; St.-Maurice et al., 1981), the plasma may experience thermal instabilities that affect the flow direction of ion irregularities.

Dimant and Oppenheim (2004) identified a theoretical ion thermal instability (ITI) by extending work on an electron thermal instability (ETI) in the upper D/lower E-region by Dimant and Sudan (1997). They predicted, using a 2-D fluid analysis, that the ITI and FBI should grow at similar wavelengths and in similar conditions, resulting in a combined instability. Kagan and Kelley (2000) also developed a theory of electron and ion thermal instabilities that could operate coincidentally with the FBI. However, Dimant and Oppenheim (2004) point out that despite qualitative similarities, a handful of quantitative differences between the two theories and incorrect estimates by Kagan and Kelley (2000) produce significant discrepancies in the results.

Both the ITI and ETI operate by heating regions of relative low plasma density and cooling regions of relatively high plasma density, increasing the magnitude of both. Since the optimum flow angle for the ITI is nonzero, it may contribute to a nonzero net flow angle of density irregularities. Unfortunately, the similar wavelength ranges of the FBI and ITI make distinguishing the ITI from the FBI in observations very challenging. Simulations may facilitate this distinction by comparing the total flow angle to that predicted by ITI theory alone.

This section follows Dimant and Oppenheim (2004) in representing the angle between the zeroth-order drift and perturbation flow as χ . The optimal angle for instability growth will be the angle at which the instability threshold is smallest, assuming fixed values for all other relevant parameters. At the altitudes of interest for this study, the optimal deviation of k from \mathbf{u}_d (toward $-\mathbf{E}_0$) for the combined instability, $\chi_{\mathrm{opt}}^{\mathrm{CI}}$, is only a few degrees, while the optimal angle between k and $\mathbf{E}_0 \times \mathbf{B}_0$ falls in the range $-10 \le \theta_{\mathrm{opt}}^{\mathrm{CI}} \le -30$.

The following set of figures show spectra of ion density perturbations in the plane perpendicular to ${\bf B}_0$ after computing the RMS over an appropriate time range. Each panel includes color-coded lines which aid in answering two questions fundamental to this work: How does the flow angle of ion perturbations change

YOUNG ET AL. 8 of 15

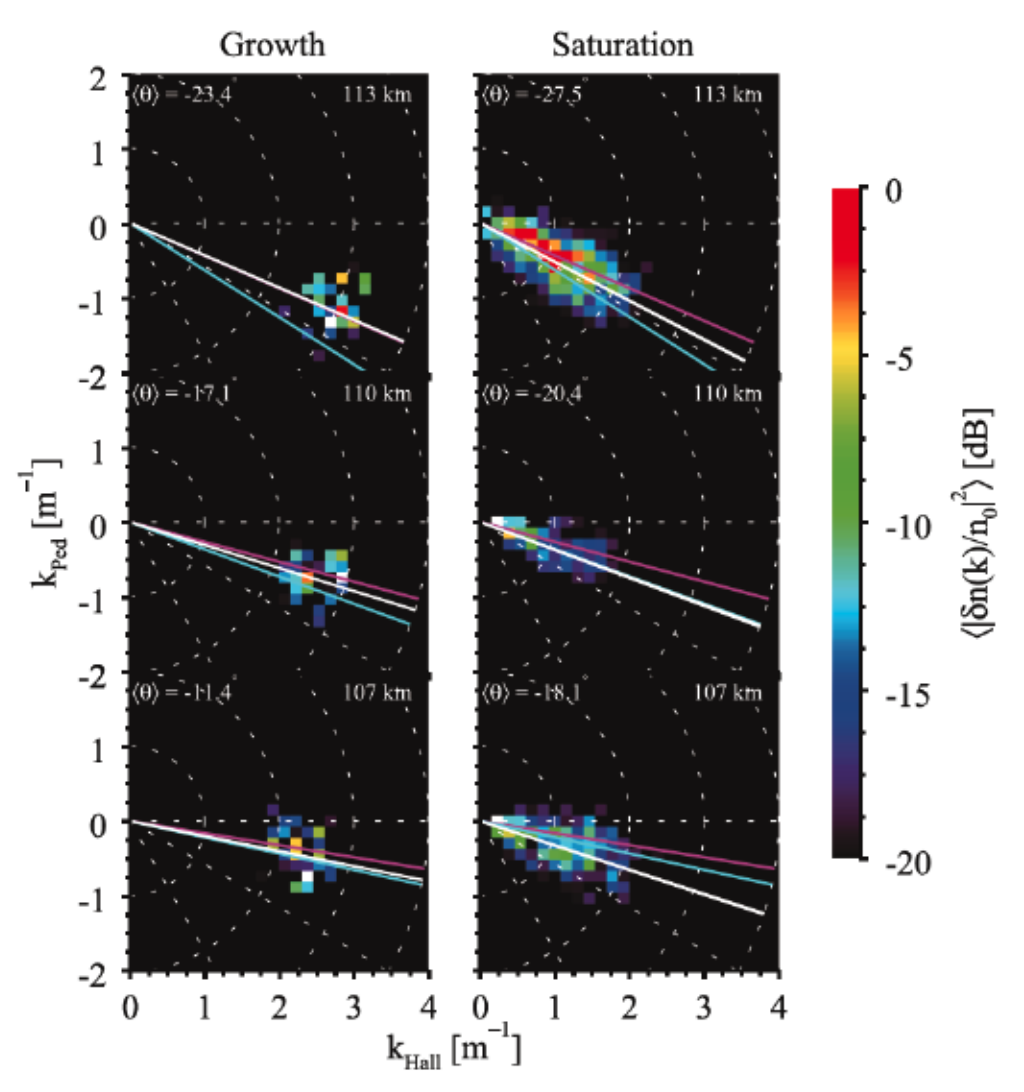


Figure 4. RMS squared spectral amplitude in density perturbations during growth and after saturation in 2-D runs. Each panel spans $0 \le k_{Hall} \le 4$ in the Hall direction and $-2 \le k_{Ped} \le +2$ in the Pedersen direction. Rows correspond to altitude, from 107 (bottom) to 113 km (top). The left column shows the growth stage, and the right column shows the saturation stage. In each panel, a magenta line indicates the drift angle, θ , a cyan line indicates the optimal flow angle for the combined FBI + ITI, $\theta_{\rm opt}$, and white lines indicate the centroid angle, $\langle \theta \rangle$, with $\pm \sigma$ uncertainties. The top left corner of each panel lists the centroid angle. The color scale for all panels ranges from -20 to 0 dB, or two orders of magnitude in power.

with altitude? Do thermal effects from the ITI significantly alter the flow angle beyond the isothermal FBI? All lines represent angles with respect to $E_0 \times B_0$.

The first line, shown in magenta, gives the angle of relative drift velocity between electrons and ions, $\mathbf{u}_d = \mathbf{u}_e - \mathbf{u}_i$. Theory predicts that the isothermal FBI growth rate should peak at the drift-velocity angle,

$$\theta = \tan^{-1} \left[-\frac{(1 + \kappa_i^2) + \Theta_0^2 (1 + \kappa_e^2)}{\kappa_e (1 + \kappa_i^2) - \Theta_0^2 (1 + \kappa_e^2) \kappa_i} \right], \tag{5}$$

where $\Theta_0 \equiv \sqrt{m_e v_e/m_t v_t}$ as in Dimant and Oppenheim (2004). See Appendix A for a derivation of ϑ .

To be relevant to a simulation run, Θ_0 must use the simulated values of its parameters. The ion mass, $m_{\ell:sim}$, is the physical ion mass, but the electron mass, $m_{\ell:sim}$, is inflated. Both ion and electron collision frequencies are as described in section 1. This work sets v_{ℓ} to maintain the appropriate value of ψ for a given altitude, accounting for the artificial electron mass. At 107 km, $\theta \approx -9^{\circ}$; at 110 km, $\theta \approx -15^{\circ}$; at 113 km, $\theta \approx -24^{\circ}$.

YOUNG ET AL. 9 of 15

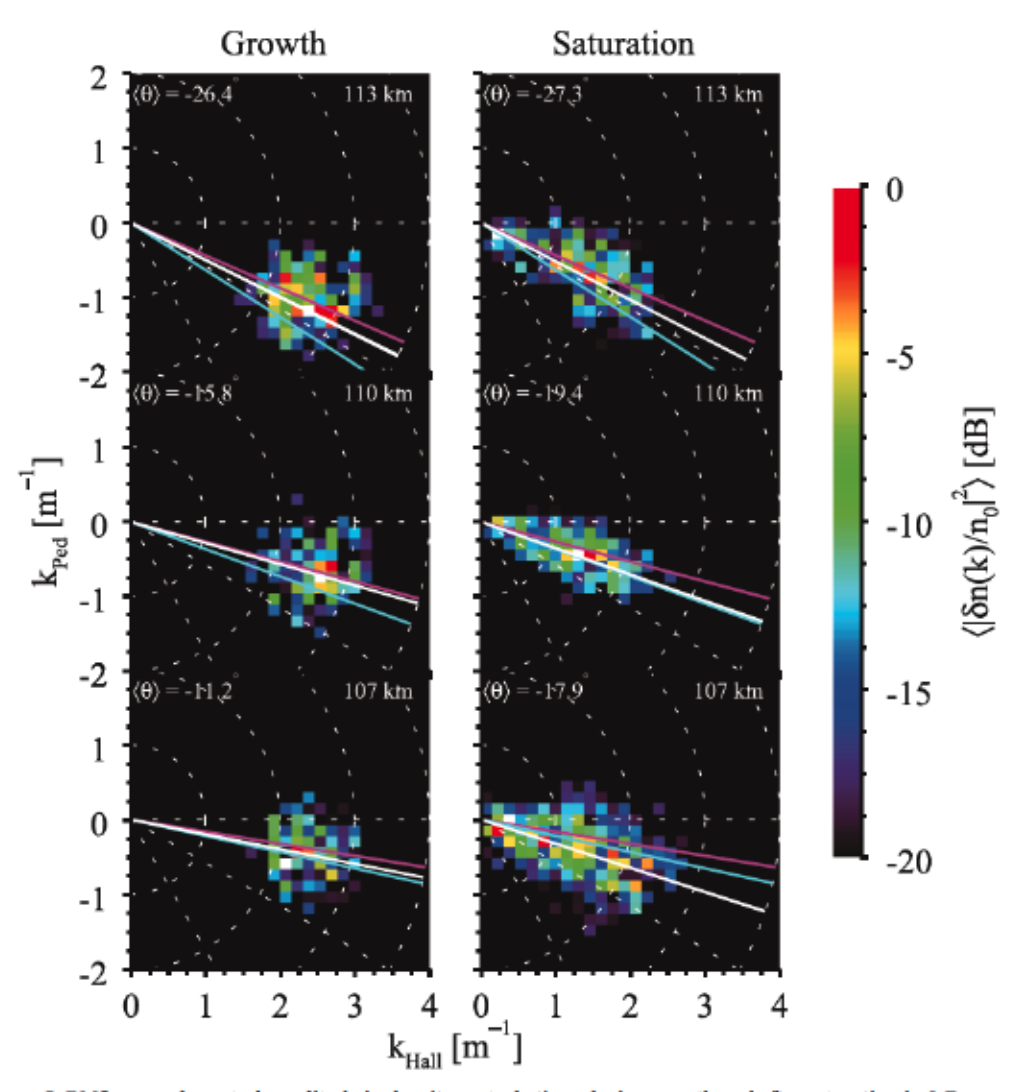


Figure 5. RMS squared spectral amplitude in density perturbations during growth and after saturation in 3-D runs. The figure layout is identical to that of Figure 4.

Estimating θ from the asymptotic values of $u_{dx:sim}$, $u_{dy:sim}$, and $u_{dz:sim}$ in the subthreshold run with $E_{y0} = 10 \text{ mV/m}$ at each altitude gives these values directly.

The second line, shown in cyan, gives the predicted deflection of FBI + ITI perturbations. Equation 34 of Oppenheim and Dimant (2004) is

$$\tan 2\chi_{\text{opt}} = -\frac{2\kappa_i (1 + \psi)}{3 - \kappa_i^2}.$$

Solving this equation for χ_{opt} and using the relation $\theta = \chi + \vartheta$ yields an equation for θ_{opt} at a given altitude:

$$\theta_{\text{opt}} = \frac{1}{2} \tan^{-1} \left[-\frac{2\kappa_i (1 + \psi)}{3 - \kappa_i^2} \right] + \theta. \tag{6}$$

This angle represents the predicted angle of maximum growth of FBI + ITI perturbations. The values are $\theta_{\rm opt} = -12^{\circ}$ at 107 km, $\theta_{\rm opt} = -20^{\circ}$ at 110 km, and $\theta_{\rm opt} = -32^{\circ}$ at 113 km. Note that, graphically, $\chi_{\rm opt}$ is the difference between the magenta and cyan lines.

The third line, shown in white, actually represents three lines: the centroid of spectral power, with plus and minus one- σ uncertainty. Since spectral power is spread over a range of angles, the angular deflection of the

YOUNG ET AL. 10 of 15

centroid of spectral power represents flow angle between the wave vector, k, and $E_0 \times B_0$. This work uses $\langle \theta \rangle$ to represent the flow angle. See Appendix B for a derivation of $\langle \theta \rangle$.

In order to reduce the uncertainty in the centroid location, the analysis routine calculated the centroid for each image in the RMS time frame, calculated $\langle \theta \rangle$ as the mean centroid from that distribution, and calculated $\delta \langle \theta \rangle$ as the standard deviation of that distribution. The standard deviation is so small in all cases as to be imperceptible in the images.

It is worth noting that the centroid is a better measure of flow angle during growth than in saturation. During the growth stage, spectral amplitude is relatively isolated in both wavelength and angle. This means that the centroid of the peak represents the peak (k_{Hall}, k_{Ped}) value of linear growth. After saturation, there is no longer a single peak wavelength that characterizes the instability. The centroid algorithm can still find the spectral center of mass, but its value as a measure of flow angle is diminished. Nonetheless, it will serve as a visual guide.

Figures 4 and 5 show $\langle |\delta n(k,\theta)/n_0|^2 \rangle$ during growth and after saturation in 2-D and 3-D runs, respectively. The data in each image correspond to the growth and saturation times in Table 2 and Figure 3. Each panel also shows the drift angle, θ , the optimum FBI + ITI flow angle, $\theta_{\rm opt}$, and the flow angle of the centroid, $\langle \theta \rangle$. Overall, the flow angle appears to be similar between 2-D and 3-D runs at a given altitude. The data resolution is poor because of the need to resolve electron dynamics: The fully kinetic simulation must resolve the Debye length, which requires grid cell sizes that are very small compared to the wavelengths of interest. Thus, most of the spectral dynamics occur close to $(k_{Hall}, k_{Ped}) = (0,0)$, where the resolution is poor. For this reason, a hybrid simulation with fluid electrons and kinetic ions would be more appropriate to this study (cf. Young et al. (2019)).

These figures show that, over the range of altitudes that this work considers, $\langle\theta\rangle$ deviates less from ϑ as altitude increases. They also show that $\langle\theta\rangle$ differs by at most a few degrees between 2-D and 3-D runs, after calculating the mean along B_0 in 3-D. Effects from the ITI are the most likely explanation for the difference between $\langle\theta\rangle$ and ϑ , especially at 110 km, where $\langle\theta\rangle$ of the saturated instability is nearly identical to $\theta_{\rm opt}$. At 107 km, $\theta_{\rm opt}$ estimates $\langle\theta\rangle$ fairly well during growth but underestimates it (in magnitude) in the saturated state. At 113 km, $|\vartheta| < |\langle\theta\rangle| \le \theta_{\rm opt}$ throughout the run. The theoretical basis presented in Dimant and Oppenheim (2004) for predicting ion thermal effects applies to 2-D perturbations in the long-wavelength limit $ku_d \ll v_l$ and does not account for kinetic effects. The shortest long-wavelength limit relevant to the simulations presented in this work is 6 m, corresponding to 107 km (assuming $|E_0| = 50$ mV/m). Therefore, the formal theory does not strictly apply to any of the simulations presented in this work. Development of a theory that describes the apparent thermal effects presented here represents an intriguing avenue of research.

5. Discussion

The results in section 4 describe the evolution of the FBI from linear to nonlinear instability. The linear instability is well established in literature and textbooks, but the precise nature of the nonlinear instability remains an open question. While the present work shows results from both 2-D and 3-D simulations, the true ionosphere is 3-D, and thus the 2-D simulations are only interesting insomuch as comparisons between 2-D and 3-D runs illustrate the fundamental role of wave modes with $k_{\parallel} \neq 0$.

It is instructive to first get an estimate of how well the overall 3-D growth rates shown in the right panel of Figure 2 compare to linear theory. Using equations (1) and (2) with parameters appropriate to 110 km, $\omega_l \approx 60 \text{ s}^{-1}$. Linear theory assumes that perturbed quantities vary as complex exponentials; thus, $\delta n/n_0 \sim \exp\left[i\left(\mathbf{k}\cdot\mathbf{r}-\omega t\right)\right]$, where **k** is the wave vector, **r** is the vector displacement, $\omega=\omega_r+i\omega_l$ is the complex frequency, and t represents time. This analysis is interested in the RMS squared amplitude of these linear perturbations, given by

$$\left\langle \left| \frac{\delta n}{n_0} \right|^2 \right\rangle \sim \exp \left(2\omega_i t \right).$$

Inserting $\omega_i \approx 60~{\rm s}^{-1}$ implies that the RMS squared amplitude should increase approximately an order of magnitude in 20 ms. The green trace in the right panels of Figure 2 confirms that this estimate is consistent with the simulation.

YOUNG ET AL. 11 of 15



The saturated 3-D spectra in Figure 3 are flat for 40.96 m $\geq \lambda > 3$ m and follow a power law with index approximately -5.0 for 3 m $> \lambda \geq 0.08$ m. In the presence of a constant driving electric field, the FBI saturates via an inverse cascade. Below the wavelength of peak growth, ion Landau damping provides a diffusion mechanism that increases with decreasing wavelength until amplitude hits the noise floor at the simulation grid scale. The steep power law fall off below $\lambda \approx 3$ m demonstrates the effectiveness of this wave-particle damping; it is a result of the sharp drop in kinetic growth rate below the wavelength of peak growth as shown in Schmidt and Gary (1973). The difference in power law index between 2-D and 3-D runs implies that 2-D simulations may overestimate the amount of wave power in perturbations with wavelengths slightly smaller than the wavelength of peak growth.

The flat spectrum at wavelengths larger than $\lambda \approx 3$ m in 3-D runs suggests a saturation mechanism independent of wavelength above the wavelength of peak growth. The instability couples energy from the wavelength of peak growth into progressively longer wavelengths until it reaches the size of the simulation box. Without a diffusion mechanism at these wavelengths, the energy stays there. The resultant saturated spectrum for all wavelengths is nearly independent of simulated altitude, implying that it depends only weakly on ν_t for the range of simulated altitudes considered here. This does not contradict the assertion by Pfaff et al. (1984) that the auroral E-region is far from homogeneous: The difference in overall growth at different altitudes (Figure 2) and the variation in growth-stage spectra (Figure 3) imply abundant variation with changing altitude.

Saturated wave power at the longest wavelengths is similar in 2-D and 3-D, but the slightly steeper slope in 2-D runs suggests that parallel modes play a role in the mode-coupling process that flattens out the 3-D spectrum. Of course, in the physical ionosphere, a nonlinear cascade of gradient-driven turbulence may steepen the apparent slope of $\langle |\delta n/n_0|^2 \rangle$ at wavelengths above the dissipation regime. The nonlinear theory of combined FBI and GDI in the equatorial electrojet proposed by Sudan (1983, 1983a) predicts a power law index of -2 to -3 at long wavelengths, with a steeper slope in the kinetic regime.

The saturated 3-D spectra in Figure 5 display significant nonzero flow angles but not necessarily significant deviations from the zeroth-order electron-ion relative drift. These spectral images predict that the flow angle of density irregularities driven by the pure FBI should increase with altitude. However, the role of thermal effects in deflecting the mean flow from $E_0 \times B_0$ will decrease with decreasing collision frequencies, so that the flow angle approaches the direction of relative drift as altitude increases. This result is qualitatively consistent with the conclusion of Uspensky et al. (2003) that the ion drift contribution to the relative drift velocity is important. Quantitatively, the calculated centroid angles in all six panels of Figure 5 are larger than the value of -10° that Uspensky et al. (2003) and Hysell et al. (2012) assume. The predicted flow angle in the saturated stage at 110 km, where many observers assume these echoes originate, is -19.4° . The theory of Dimant and Oppenheim (2004) predicts this value quite well.

By comparing linear fluid theory to linear kinetic theory in the long-wavelength limit, Wang and Tsunoda (1975) showed that the optimum aspect angle is a few tenths of a degree for electron drift speeds around 600 m/s and increases as electron drift speed increases. Schlegel (1983) ran a numerical analysis with $\lambda \approx 1$ m at 110 km and showed that the optimum aspect angle does not increase monotonically with drift speed but reaches a maximum for a drift speed of 1.4 km/s. The FBI produces predominantly field-aligned irregularities (Makarevich, 2009), but some observers have reported observations at aspect angles of 1° and larger (cf. Haldoupis, 1989).

During the growth phase of the simulations presented here, perturbations had a wavelength of approximately 3 m in the perpendicular plane. Spectra that included k_{\parallel} (not shown) contained power in the lowest nonzero k_{\parallel} pixel, corresponding to $k_{\parallel}=2\pi/L_z$. Since the parallel resolution is also $2\pi/L_z$, that results in a growth-stage aspect angle of approximately 1°-2° off perpendicular. For comparison, the theoretical simulated value is $\Theta_{0:slm}=\sqrt{m_{e:slm}v_{e:slm}/m_{l}v_{l:slm}}\approx 1.7^{\circ}$ and the theoretical physical value is $\Theta_{0}=\sqrt{m_{e}v_{e}/m_{l}v_{l}}\approx 1.1^{\circ}$. Therefore, the simulation appears to model parallel modes reasonably well for the given parameters.

6. Summary

This paper presents 2-D and 3-D fully kinetic simulations of the Farley-Buneman instability in the high-latitude ionosphere, at three different simulated altitudes: 107, 110, and 113 km. The middle simulated

YOUNG ET AL. 12 of 15



altitude corresponds to the assumed altitude of many observed auroral radar echoes. Mean irregularity amplitude at all wavelengths over the course of each run exhibits a linear growth phase followed by a saturated phase. The linear growth phase at 113 km starts off slower than at 107 and 110 km in 2-D runs, and growth is slower overall in 2-D runs when compared to 3-D runs.

Snapshots of amplitude versus wave number for 2-D and 3-D runs demonstrate different growth behavior for each set: While the primary wavelength of irregularity growth is a few meters in all runs, the 3-D run at 113 km contains a secondary wavelength of peak growth at the sub-meter scale. At all altitudes, 2-D runs show earlier long-wavelength growth. The saturated stage of 2-D runs exhibits a power law with slopes -3.3 to -4.1 at meter scales and a shallower slope at longer wavelengths. The saturated stage of 3-D runs exhibits a power law with slopes -4.8 to -5.5 at meter scales and a nearly flat spectrum at longer wavelengths.

Images in the perpendicular plane show that the mean irregularity flow angle is never 0° at these altitudes and that the flow angle increases from growth to saturation. The deflection from 0° results from a combination of thermal effects and the zeroth-order direction of electron-ion relative flow. The flow angle of the saturated instability increases with increasing altitude, but thermal effects appear to decrease with increasing altitude, so that the mean flow approaches the relative drift with increasing altitude. Overall, this work predicts that the saturated amplitude of Farley-Buneman irregularities should exhibit a flat spectrum with a knee near the wavelength of peak growth and a flow angle at least as large as, and probably a few degrees larger than, the deviation of relative drift from $E_0 \times B_0$.

Appendix A: Drift Angle

In the absence of pressure gradients and inertia, assuming $\mathbf{E}_0 = E_0 \hat{y}$ and $\mathbf{B}_0 = B_0 \hat{z}$, the drift components of species s are

$$u_{sy} = \frac{q_s E_0}{v_s m_s (1 + \kappa_s^2)},$$
 (A1)

$$u_{xx} = \kappa_s u_{sy} = \frac{\kappa_s q_s E_0}{\nu_s m_s (1 + \kappa_s^2)}.$$
 (A2)

The drift-velocity components are thus

$$u_{dy} = u_{dy} - u_{dy} \tag{A3}$$

$$= +eE_0 \left[\frac{\kappa_e}{m_e \nu_e \left(1 + \kappa_e^2 \right)} - \frac{\kappa_l}{m_l \nu_l \left(1 + \kappa_i^2 \right)} \right], \tag{A4}$$

$$u_{dy} = u_{ey} - u_{ly} \tag{A5}$$

$$= -eE_0 \left[\frac{1}{m_e v_e (1 + \kappa_e^2)} + \frac{1}{m_i v_i (1 + \kappa_i^2)} \right]. \tag{A6}$$

These components make an angle $\theta = \tan^{-1}(u_{dy}/u_{dx})$ with the $E_0 \times B_0$ (i.e., \hat{x}) direction. Plugging in the above expressions for u_{dx} and u_{dy} yields the expression for θ given in section 4.2

Appendix B: Centroid Angle

Consider a 2-D discrete distribution, $f(x_l, y_j)$, with $x_l = i\Delta x$, $y_j = j\Delta y$ and $(i, j) \in \{0..N_x - 1\} \otimes \{0..N_y - 1\}$. The coordinates of the center of mass, $(\langle x \rangle, \langle y \rangle)$, are

$$\langle x \rangle = \frac{\sum\limits_{j} \sum\limits_{l} x_{l} f(x_{l}, y_{j})}{\sum\limits_{j} \sum\limits_{l} f(x_{l}, y_{j})} = \frac{1}{M} \sum\limits_{j} \sum\limits_{l} x_{l} f_{lj}, \tag{B1}$$

YOUNG ET AL. 13 of 15

$$\langle y \rangle = \frac{\sum_{i} \sum_{j} y_{j} f(x_{i}, y_{j})}{\sum_{i} \sum_{j} f(x_{i}, y_{j})} = \frac{1}{M} \sum_{i} \sum_{j} y_{j} f_{ij},$$
(B2)

where $f_{ij} \equiv f(x_i, y_j)$ and $M \equiv \sum_j \sum_i f_{ij}$ is the total mass. These are just the components of the first moment of the distribution with respect to the radial coordinate $r \equiv (x, y)$.

The conversion from Cartesian to polar coordinates is straightforward: $\langle k \rangle = \sqrt{\langle x \rangle^2 + \langle y \rangle^2}$ and $\langle \theta \rangle = \tan^{-1}(\langle y \rangle / \langle x \rangle)$.

Acknowledgments

comments.

NASA Grant NNX14AI13G supported the research presented in this work. This work used TACC and XSEDE computational resources supported by NSF Grant ACI-1053575. This paper did not use any data. Simulation runs are archived on the TACC Ranch system. TACC account holders who would like to directly access the raw simulation output should contact the corresponding author. The simulation source code and input files used to produce the runs presented in this work are archived at http://doi.org/10. 5281/zenodo.3595372. The authors thank the reviewers for constructive

References

Booker, H. G. (1956). A theory of scattering by nonisotropic irregularities with application to radar reflections from the aurora. Journal of Atmospheric and Solar-Terrestrial Physics, 8, 204–221. http://doi.org/10.1016/0021-9169(56)90126-X

Bowles, K. L. (1954). Doppler shifted radio echoes from aurora. Journal of Geophysical Research, 59, 553–555. http://doi.org/10.1029/ JZ059i004p00553

Bowles, K. L., Balsley, B. B., & Cohen, R. (1963). Field-aligned e-region irregularities identified with acoustic plasma waves. Journal of Geophysical Research, 68(9), 2485–2501. http://doi.org/10.1029/JZ068i009p02485

Bowles, K. L., Cohen, R., Ochs, G. R., & Balsley, B. B. (1960). Radio echoes from field-aligned ionization above the magnetic equator and their resemblance to auroral echoes. *Journal of Geophysical Research*, 65(6), 1853–1855. http://doi.org/10.1029/JZ065i006p01853

Buneman, O. (1963). Excitation of field aligned sound waves by electron streams. Physical Review Letters, 10, 285.

Cohen, R., & Bowles, K. (1963). The association of planeaXRwave electronaXRdensity irregularities with the equatorial electrojet. Journal of Geophysical Research, 68(9), 2503–2525. http://doi.org/10.1029/JZ068i009p02503

Dimant, Y. S., & Oppenheim, M. M. (2004). Ion thermal effects on E-region instabilities: Linear theory. Journal of Atmospheric and Solar-Terrestrial Physics, 66, 1639–1654.

Dimant, Y. S., & Oppenheim, M. M. (2011a). Magnetosphere-ionosphere coupling through E-region turbulence: 1. Energy budget. *Journal of Geophysical Research*, 116, A09303. http://doi.org/10.1029/2011JA016648

Dimant, Y. S., & Oppenheim, M. M. (2011b). Magnetosphere-ionosphere coupling through E-region turbulence: 2. Anomalous conductivities and frictional heating. *Journal of Geophysical Research*, 116, A09304. http://doi.org/10.1029/2011JA016649

Dimant, Y. S., & Sudan, R. N. (1995). Kinetic theory of the Farley-Buneman instability in the E-region of the ionosphere. Journal of Geophysical Research, 100, 14,605–14,624. http://doi.org/10.1029/95JA00794

Dimant, Y. S., & Sudan, R. N. (1997). Physical nature of a new cross-field current-driven instability in the lower ionosphere. Journal of Geophysical Research, 102, 2551–2564. http://doi.org/10.1029/96JA03274

Eckersley, T. L. (1937). Irregular ionic clouds in the E layer of the ionosphere. Nature, 140, 846–847. http://doi.org/10.1038/140846a0 Farley, D. T. (1963a). A plasma instability resulting in field-aligned irregularities in the ionosphere. Journal of Geophysical Research, 68,

Farley, D. T. (1963b). Two-stream plasma instability as a source of irregularities in the ionosphere. Physical Review Letters, 10(7), 279–282.
Farley, D. T. (2009). The equatorial E-region and its plasma instabilities: A tutorial. Annales Geophysicae, 27, 1509–1520. http://doi.org/10.5194/angeo-27-1509-2009

Fejer, B. G., & Kelley, M. C. (1980). Ionospheric irregularities. Reviews of Geophysics and Space Physics, 18, 401–454. http://doi.org/10.1029/RG018i002p00401

Foster, J., & Erickson, P. (2000). Simultaneous observations of E-region coherent backscatter and electric field amplitude at F-region heights with the millstone hill UHF radar. Geophysical Research Letters, 27(19), 3177–3180. http://doi.org/10.1029/2000GL000042

Haldoupis, C. (1989). A review on radio studies of auroral E-region ionospheric irregularities. Annales Geophysicae, 7, 239–258.

Haldoupis, C., Nielsen, E., & Ierkic, H. M. (1984). STARE Doppler spectral studies of westward electrojet radar aurora. Planetary and Space Science, 32, 1291–1300. http://doi.org/10.1016/0032-0633(84)90072-2

Hysell, D. L. (2015). The radar aurora, Auroral dynamics and space weather (pp. 191–209). Washington, DC: American Geophysical Union (AGU). http://doi.org/10.1002/9781118978719.ch14

Hysell, D., Miceli, R., Munk, J., Hampton, D., Heinselman, C., Nicolls, M., et al. (2012). Comparing VHF coherent scatter from the radar aurora with incoherent scatter and all-sky auroral imagery. *Journal of Geophysical Research*, 117, A10313. http://doi.org/10.1029/ 20121A018010

Iranpour, K., Pécselí, H. L., Trulsen, J., Bahnsen, A., Primdahl, F., & Rinnert, K. (1997). Propagation and dispersion of electrostatic waves in the ionospheric E-region. Annales Geophysicae, 15(7), 878–889. http://doi.org/10.1007/s00585-997-0878-4

Janhunen, P. (1994a). Implications of flow angle stabilization on coherent E-region spectra. Journal of Geophysical Research, 99, 13. http://doi.org/10.1029/94JA00894

Janhunen, P. (1994b). Perpendicular particle simulation of the E-region Farley-Buneman instability. Journal of Geophysical Research, 99, 11,461–11,474. http://doi.org/10.1029/94JA00206

Kagan, L. M., & Kelley, M. C. (2000). A thermal mechanism for generation of small-scale irregularities in the ionospheric E-region. Journal of Geophysical Research, 105, 5291–5302. http://doi.org/10.1029/1999JA900415

Kelley, M. C., & Mozer, F. S. (1973). Electric field and plasma density oscillations due to the high-frequency Hall current two-stream instability in the auroral E-region. *Journal of Geophysical Research*, 78(13), 2214–2221. http://doi.org/10.1029/JA078i013p02214

Mäseide, K., Holtet, J. A., Egeland, A., & Maynard, N. C. (1973). Electric field and fine structure in aurora. Journal of Atmospheric and Solar-Terrestrial Physics, 35, 1833–1841. http://doi.org/10.1016/0021-9169(73)90057-3

Makarevich, R. A. (2009). Coherent radar measurements of the doppler velocity in the auroral E-region. URSI Radio Science Bulletin, 2009(328), 33–46. http://doi.org/10.23919/URSIRSB.2009.7909539

Makarevich, R. A. (2016a). Toward an integrated view of ionospheric plasma instabilities: 2. Three inertial modes of a cubic dispersion relation. Journal of Geophysical Research: Space Physics, 121, 6855–6869. http://doi.org/10.1002/2016JA022864

Makarevich, R. A. (2016b). Toward an integrated view of ionospheric plasma instabilities: Altitudinal transitions and strong gradient case. Journal of Geophysical Research: Space Physics, 121, 3634–3647. http://doi.org/10.1002/2016JA022515

YOUNG ET AL. 14 of 15

- Makarevich, R. A. (2019). Toward an integrated view of ionospheric plasma instabilities: 3. Explicit growth rate and oscillation frequency for arbitrary altitude. Journal of Geophysical Research: Space Physics, 124, 6138–6155. http://doi.org/10.1029/2019JA026584
- Nielsen, E., & Schlegel, K. (1983). A first comparison of STARE and EISCAT electron drift velocity measurements. Journal of Geophysical Research, 88(A7), 5745–5750. http://doi.org/10.1029/JA088iA07p05745
- Nielsen, E., & Schlegel, K. (1985). Coherent radar doppler measurements and their relationship to the ionospheric electron drift velocity. Journal of Geophysical Research, 90(A4), 3498–3504. http://doi.org/10.1029/JA090iA04p03498
- Nielsen, E., & Schmidt, W. (2014). The STARE/SABRE story. History of Geo- and Space Sciences, 5(1), 63–72. http://doi.org/10.5194/ hgss-5-63-2014
- Oppenheim, M. M., & Dimant, Y. S. (2004). Ion thermal effects on E-region instabilities: 2D kinetic simulations. Journal of Atmospheric and Solar-Terrestrial Physics, 66, 1655–1668. http://doi.org/10.1016/j.jastp.2004.07.007
- Oppenheim, M. M., & Dimant, Y. S. (2013). Kinetic simulations of 3-D Farley-Buneman turbulence and anomalous electron heating. Journal of Geophysical Research: Space Physics, 118, 1306–1318. http://doi.org/10.1002/jgra.50196
- Oppenheim, M. M., Dimant, Y., & Dyrud, L. P. (2008). Large-scale simulations of 2-D fully kinetic Farley-Buneman turbulence. Annales Geophysicae, 26, 543-553. http://doi.org/10.5194/angeo-26-543-2008
- Pfaff, R. F., Kelley, M. C., Fejer, B. G., Kudeki, E., Carlson, C. W., Pedersen, A., & Hausler, B. (1984). Electric field and plasma density measurements in the auroral electrojet. *Journal of Geophysical Research*, 89(A1), 236–244. http://doi.org/10.1029/JA089iA01p00236
- Pfaff, R. F., Sahr, J., Providakes, J. F., Swartz, W. E., Farley, D. T., Kintner, P. M., et al. (1992). The E-region Rocket/Radar Instability Study (ERRRIS)—Scientific objectives and campaign overview. *Journal of Atmospheric and Solar-Terrestrial Physics*, 54(6), 779–808. http://doi.org/10.1016/0021-9169(92)90116-3
- Rosenberg, M., & Chow, V. W. (1998). Farley-Buneman instability in a dusty plasma. Planetary and Space Science, 46, 103–108. http://doi.org/10.1016/S0032-0633(97)00104-9
- Sahr, J. D., Farley, D. T., Swartz, W. E., Providakes, J. F., & Pfaff, R. F. (1992). Observations of 3-m auroral irregularities during the ERRRIS campaigns. Journal of Atmospheric and Solar-Terrestrial Physics, 54(6), 809–818. http://doi.org/10.1016/0021-9169(92)90117-4
- Sahr, J. D., & Fejer, B. G. (1996). Auroral electrojet plasma irregularity theory and experiment: A critical review of present understanding and future directions. Journal of Geophysical Research, 101(A12), 26,893–26,910. http://doi.org/10.1029/96JA02404
- Schlegel, K. (1983). Interpretation of auroral radar experiments using a kinetic theory of the two-stream instability. Radio Science, 18(1), 108-118. http://doi.org/10.1029/RS018i001p00108
- Schlegel, K., & St.-Maurice, J. P. (1981). Anomalous heating of the polar E-region by unstable plasma waves. I—Observations. Journal of Geophysical Research, 86, 1447–1452. http://doi.org/10.1029/JA086iA03p01447
- Schmidt, M. J., & Gary, S. P. (1973). Density gradients and the Farley-Buneman instability. Journal of Geophysical Research, 78, 8261–8265. http://doi.org/10.1029/JA078i034p08261
- Schunk, R. W., & Nagy, A. F. (2004). Ionospheres. Cambridge: Cambridge University Press.
- St.-Maurice, J.-P., & Hamza, A. M. (2001). A new nonlinear approach to the theory of E-region irregularities. Journal of Geophysical Research, 106, 1751–1760. http://doi.org/10.1029/2000JA000246
- St.-Maurice, J. P., Schlegel, K., & Banks, P. M. (1981). Anomalous heating of the polar E-region by unstable plasma waves. II—Theory. Journal of Geophysical Research, 86, 1453–1462. http://doi.org/10.1029/JA086iA03p01453
- Sudan, R. N. (1983). Unified theory of type I and type II irregularities in the equatorial electrojet. Journal of Geophysical Research, 88, 4853–4860. http://doi.org/10.1029/JA088iA06p04853
- Sudan, R. N. (1983a). Nonlinear theory of type I irregularities in the equatorial electrojet. Geophysical Research Letters, 10, 983–986. http://doi.org/10.1029/GL010i010p00983
- Uspensky, M., Koustov, A., Janhunen, P., Pellinen, R., Danskin, D., & Nozawa, S. (2003). STARE velocities: The importance of off-orthogonality and ion motions. Annales Geophysicae, 21, 729-743. http://doi.org/10.5194/angeo-21-729-2003
- Wang, T. N. C., & Tsunoda, R. T. (1975). On a crossed field two-stream plasma instability in the auroral plasma. Journal of Geophysical Research, 80(16), 2172. http://doi.org/10.1029/JA080i016p02172
- Young, M. A., Oppenheim, M. M., & Dimant, Y. S. (2019). Simulations of secondary Farley-Buneman instability driven by a kilometer-scale primary wave: Anomalous transport and formation of flat-topped electric fields. *Journal of Geophysical Research: Space Physics*, 124, 734–748. https://doi.org/10.1029/2018JA026072

YOUNG ET AL. 15 of 15